Available online at www.sciencedirect.com
ScienceDirect

Journal of the European Ceramic Society 28 (2008) 3155–3164

www.elsevier.com/locate/jeurceramsoc

Degradation of TiB_2 ceramics in liquid aluminum

M.S. Jensen [a,1], M. Pezzotta [b,1], Z.L. Zhang [b],
M.-A. Einarsrud [a], T. Grande [a,*]

[a] *Department of Materials Science and Engineering, Norwegian University of Science and Technology (NTNU), N-7491 Trondheim, Norway*
[b] *Department of Structural Engineering, Norwegian University of Science and Technology (NTNU), N-7491 Trondheim, Norway*

Received 12 February 2008; received in revised form 30 April 2008; accepted 9 May 2008
Available online 24 June 2008

Abstract

Infiltration of liquid aluminum in three TiB_2 materials with significantly different microstructures at 1000 °C has been studied. The results show large differences in resistance towards aluminum penetration. A TiB_2 material containing transition metal sintering aid, displayed a low resistance towards penetration of liquid aluminum along grain boundaries. Grain boundary penetration was also observed in a second material containing an oxycarbide secondary phase $TiC_{1-x}O_x$, while Al infiltration could not be detected after 100 h, in a third material with apparently no secondary phases. The flexural strength, hardness and stiffness of the exposed material showing the lowest resistance towards penetration of aluminum, decreased due to penetration along grain boundaries, and the fracture mode changed from transgranular to intergranular. The experimental observations were analyzed using a two-dimensional finite element model, reproducing the observed reduction in the stiffness due to aluminum infiltration.

Keywords: TiB_2; Corrosion; Al; Grain boundaries; Infiltration; Fracture

1. Introduction

Titanium diboride (TiB_2) is the prime candidate as a drained and inert cathode material in Hall–Héroult aluminum electrolysis cells.[1–4] Despite the potential of TiB_2 materials, inert cathodes based on TiB_2 have still to be demonstrated in industrial cells. The main challenge is related to the fabrication and the properties of TiB_2 polycrystalline materials. Sintering of TiB_2 is a challenge due to the high melting point (~3000 °C), and a very fine powder, sintering aids or hot pressing are necessary in order to obtain high density and at the same time control grain growth during sintering.[5–8] Controlling the grain growth is important since microcracking is known to occur above a critical grain size.[9,10] TiB_2 exposed to air is always covered by an oxide scale due to oxidation, and TiB_2 ceramics free of oxide impurities are difficult to achieve. Moreover, despite the low solubility of TiB_2 in liquid aluminum,[11] TiB_2 ceramics are vulnerable to penetration of liquid aluminum along grain boundaries.[12–20] The resistance towards infiltration of aluminum along grain boundaries is most likely dependent on the microstructure of the materials, especially the impurity level and composition at the grain boundaries, the grain size, and finally the porosity and the degree of microcracking.[12–20] The degradation mechanism of TiB_2 during exposure to liquid aluminum has some common features of liquid metal-induced embrittlement (LMIE or LME)[21] however, Al penetration in TiB_2 is different from LMIE due to the low solubility of TiB_2 in Al and the lack of ductility of solid TiB_2. For metal–metal systems the embrittled solid metal fractures at a lower strain,[21] while a softening of TiB_2 is anticipated by Al grain boundary infiltration due to the ductile nature of Al. The excellent wetting of TiB_2 by Al,[3] indicates that the wetting and spreading processes are far too rapid to have a large influence on the much slower grain boundary infiltration restricted by the low solubility of TiB_2 in Al.

Here, we present a study of the infiltration of liquid aluminum in three TiB_2 materials with different secondary phases, density and microstructures. Moreover, the mechanical properties of one partly infiltrated TiB_2 material were investigated by four

---

[*] Corresponding author.
E-mail address: Tor.Grande@material.ntnu.no (T. Grande).

[1] M.S. Jensen has performed most of the experimental data reported here, while M. Pezzotta has performed the finite element method simulations.

0955-2219/$ – see front matter © 2008 Elsevier Ltd. All rights reserved.
doi:10.1016/j.jeurceramsoc.2008.05.011

point bending, and the experimental data was modeled using numerical simulations.

2. Experimental

2.1. Materials

Three different TiB_2 materials from external suppliers were used, material C (Ceradyne Inc., Costa Mesa, CA, USA), material W (Wacker Chemie AG, München, Germany) and finally material H (Norsk Hydro ASA, Oslo, Norway). Materials C and W are commercial materials, while material H was produced by Hydro Research Laboratories in Porsgrunn, Norway. Materials C and H were fabricated by hot pressing (HP), while material W was produced by conventional sintering. More information about the materials is given in Table 1.

2.2. Exposure to liquid aluminum

Four point (4-pt) bending test bars (described below) were placed in an alumina crucible between two aluminum blocks of ∼75 g and heated to 1000 °C followed by immediate cooling to ambient temperature (heating/cooling rate 10 °C/min) in a graphite furnace filled with Argon. This first heating cycle in inert atmosphere was performed in order to obtain a complete Al coverage of the bars. The following exposure to Al were performed in a muffle furnace at 1000 °C in air so that the crucible could be turned up-side down to separate the bars from molten Al after exposure. However, due to oxidation of liquid Al, which further resulted in oxidation of the bars and would thereby influence on the interaction with molten aluminum, the exposure time was limited to <24 h. Therefore, for exposure times >24 h, test bars were held at 1000 °C for longer times in the graphite furnace filled with Argon, before reheating in the muffle furnace and separation from the liquid Al by the same procedure. After the exposure, the remaining Al at the surface of the bars was removed first by etching in HCl followed by polishing using SiC papers (Struers FEPA P#500–P#1000).

2.3. Mechanical characterization

4-Pt bending bars (3 mm × 4 mm × 50 mm) were prepared according to the ASTM C 1161–2002 standard with the B configuration. Flexural strength of the unexposed and exposed bars was measured at room temperature using a 4-pt bending test arrangement with a fully articulating 40/20 span SiC bend fixture (MTS Model 642.85) placed between two SiC pushrods attached to a 20 kN electrochemical machine (Cormet) and a 2 kN load cell (HBN). Deflection of the specimens during loading was measured with a bend bar extensiometer (MTS Model 632.70-03) with three extensiometer pushrods (MTS Model 602.81). The two outer pushrods were placed in correspondence with the two upper rollers of the bend fixture, while the third was placed in the center of the sample. The deflection was taken as the difference in movement between the center rod and the outer rods. Normally 3 test bars were measured for each exposure time.

After testing, the bars were cut using an automatic cut-off machine (Struers Accutom-5, Ballerup, Denmark) using a diamond blade to obtain a cross section of the specimens. The cross sections were ground and polished to a mirror like finish using the procedure described in Struers e-Metal for preparation of TiB_2 ceramics.

Vickers indentation tests were carried out on the polished cross sections using a Leica VMHT Mot microhardness tester (Wetzlar, Germany). Loads between 0.981 and 19.62 N were applied, the loading rate was 25 μm/s and the holding time was 10 s. The indents were measured using SEM (Hitachi S-3500N). Normally 4 indents for each load were used to calculate hardness.

2.4. Characterization of the microstructure

Polished cross sections of the tested bars and fracture surfaces of the bars were investigated using a Hitachi S-3500N scanning electron microscope (SEM, Ibaraki, Japan) attached with an energy dispersive spectrometer (EDS, Oxford Inc., Abingdon, UK) and a digital electron backscatter diffraction (EBSD) detector (Nordif, Trondheim, Norway). An electron probe microanalyzer (EPMA, Jeol JXA-8500F, Tokyo, Japan) was used for element analysis of the secondary phases. X-ray diffraction (XRD) of the 4 mm × 50 mm surface of the bars was performed using a Bruker AXE D8 Advance X-ray diffractometer (Karlsruhe, Germany) using Cu Kα radiation and a VANTEC-1 detector. A stepsize of 0.082° and a counting time of 1 s were used in the 2θ range 25–70°. The density of the materials was measured using Archimedes method in isopropanol.

2.5. Finite element modeling

Finite element (FE) calculations were performed to predict the mechanical properties of the exposed TiB_2. A two-dimensional model of the 4-pt bending specimen was used, and considering the geometry of the specimen,[22] plane strain was assumed. Since both the geometry and the applied load were symmetric, only half of the specimen as shown in Fig. 1 was

Table 1
Density, grain size, secondary phases and flexural strength of materials C, H and W

Sample	Density (%)	Grain size (μm)	Secondary phases	Flexural strength (MPa)
C	98.0	7.6 (250)[a]	$Ti_{0.50}N_{0.27}O_{0.12}C_{0.11} + B_{0.22}N_{0.21}Co_{0.19}Ni_{0.16}Fe_{0.16}Ti_{0.04}Cr_{0.02}$[b]	411 ± 152
H	94.5	10.5 (394)[a]	–	293 ± 6
W	99.0	16.6 (365)[a]	$Ti_{0.48}N_{0.25}O_{0.16}C_{0.11}$	273 ± 18

[a] Number of measured grains are included in parenthesis.

[b] Metallic phase.

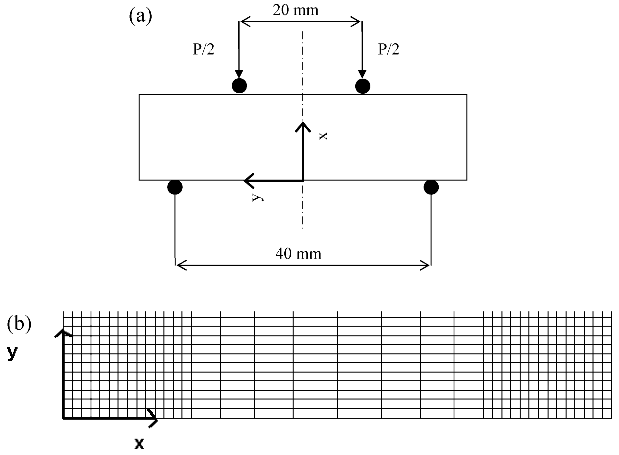

Fig. 1. Schematic representation of the (a) 4 point bending setup and (b) FE model of half the 4 point bending specimen with zoom at the *x*-axis.

modeled. The commercial FE program ABAQUS was used for the analysis and a model with 18,000 elements was employed after evaluation of the effects of different mesh refinement levels.

The two scenarios for the penetration of Al in the polycrystalline samples used in the modeling are illustrated in Fig. 2. Two different types of grain boundary representation were considered: straight-lines (Fig. 2a) and zig-zag pattern (Fig. 2b). Considering the model in Fig. 2a, the infiltrated grain boundaries in TiB_2 were modeled by sets of consecutive elements with the mechanical properties of aluminum. The sets were parallel to each other and the length of the sets in the specimen was the same and corresponded to the penetration depth, *a* (Fig. 2a) Al penetration was considered at both sides of the model. Three penetration depths were used: 0.2, 0.45 and 0.65 mm, respectively reflecting the experimental data for material C. The distance along the *y*-direction between one set and the next one, *d*, is related to the Al volume content in the specimen. Fundamental parameters of the analysis were the penetration depth, the Al equivalent volume percentage, v, and the grain boundary thickness, *t* (see Fig. 2). The equivalent volume percentage of Al present in the specimen was calculated as the ratio between the volume of Al elements and the volume of the specimen. Due to computational simplifications the grain boundary thickness, *t*, employed in the FE analyses was larger than in reality. A brief analysis of the effect of the grain boundary thickness on the simulated specimen stiffness was carried out. The effect of the grain boundary pattern on the specimen stress distribution was also analyzed by considering the zig-zag model in Fig. 2(b). A similar model has been developed by Chawla and Sidhu[23] to characterize the influence of the microstructure on the mechanical properties of the composite Sn-rich solder-Cu system with intermetallics.

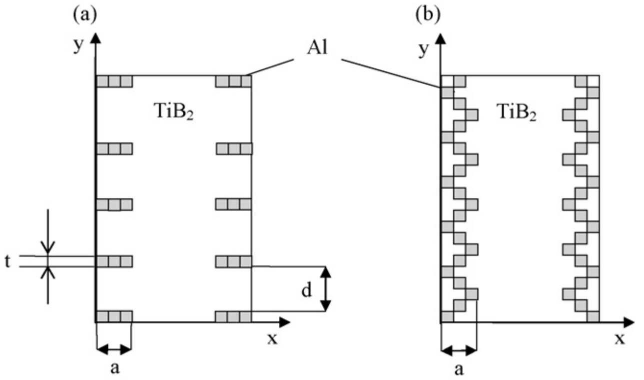

Fig. 2. The two scenarios considered in the FE analyses: (a) half specimen with straight Al-infiltrated grain boundaries and (b) half specimen with zig-zag Al-infiltrated grain boundaries. The shaded area represents the aluminum, *t* is the grain boundary (and element) thickness, *a* is the penetration depth and *d* is the distance between two consecutive grain boundaries measured along the *y*-axis.

In the present model, the average material properties of TiB_2 were assigned to the specimen and elastic isotropy was assumed. The Al is assumed to be elastic with Young's modulus of 71 GPa and a Poisson ratio of 0.3.[24]The Young's modulus of TiB_2 is 732 GPa, which was obtained from the 4-pt bending of the pristine TiB_2 specimens. The Poisson ratio adopted for TiB_2 was 0.108.[25]

3. Results

3.1. Microstructure of the pristine materials

SEM micrographs of the unexposed materials C, H and W are shown in Fig. 3. The three TiB_2 materials had significantly different densities and microstructures with respect to average grain size and content of secondary phases. The density, microstructural features and the flexural strength of the materials are summarized in Table 1. The secondary phase in material C can be seen as bright spots located at the grain boundaries in Fig. 3a. EDS analysis revealed that this secondary phase, consisted mainly of the transition metals Cr, Ni, Fe, Co in addition to Ti. EPMA showed that there were two different secondary phases in the material, a Ti–N–O–C phase and the phase containing transition metals. The transition metals originated from the sintering aid used to promote densification. Material C with a high density and small grain size showed the highest flexural strength. No secondary phases were observed in material H. This material had an intermediate grain size compared to the two others and a lower flexural strength than material C due to a higher porosity. Material W contained a secondary phase that can be seen in the micrograph as brighter inclusions located at the grain boundaries (Fig. 3c). EDS revealed that the secondary phase consisted of mainly Ti, C and O, corresponding to a titanium monocarboxide $TiC_{1-x}O_x$. EPMA showed that the secondary phase was a Ti–N–O–C phase. Microcracks induced by the anisotropic thermal expansion of TiB_2 can be seen in material W (Fig. 3c), which also explains the low mechanical strength of this material. Microcracking was only observed in the material with the largest grain size (material W) in line with expectations.

XRD data of the three materials are shown in Fig. 4. The two diffraction lines due to secondary phases observed for material C and W could be indexed to a face-centered cubic structure with unit cell parameters 4.307 ± 0.011 and 4.287 ± 0.005 Å, respectively, which is in between what is reported by Afir et

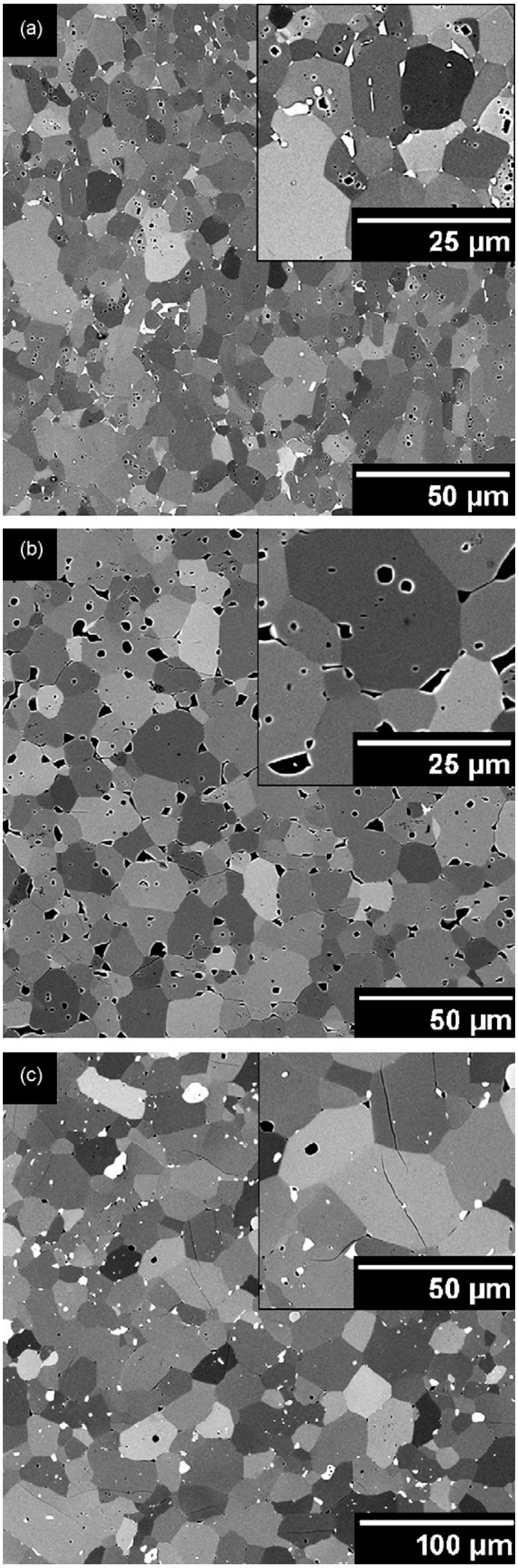

Fig. 3. SEM micrographs (BSE) of the pristine TiB_2 materials (a) material C, (b) material H and (c) material W.

al.[26] for TiO and TiC, both with rock salt structures. Based on XRD and EPMA it can be concluded that the Ti–O–C–N phase in materials C and W is a solid solution of TiO, TiC and TiN with rock salt structure. The relative intensities of the Bragg reflections for materials C and H were not in accordance with the ICDD powder diffraction file for TiB_2 (Pattern: 00-035-0741). This is due to preferential grain orientation during sintering as recently has been reported for hot pressed TiB_2 by Jensen et al.[27] The intensity of the reflections in the diffractograms indicate that the bars were oriented so that the grains tend to have the [0 0 1] direction normal to the 4 mm × 50 mm surface which was therefore normal to the hot pressing direction.

3.2. Exposure to molten aluminum

The materials C, W and H were exposed for various times in liquid aluminum at 1000 °C. Our first attempt was to identify Al penetration by EDS analysis, but it was not possible to

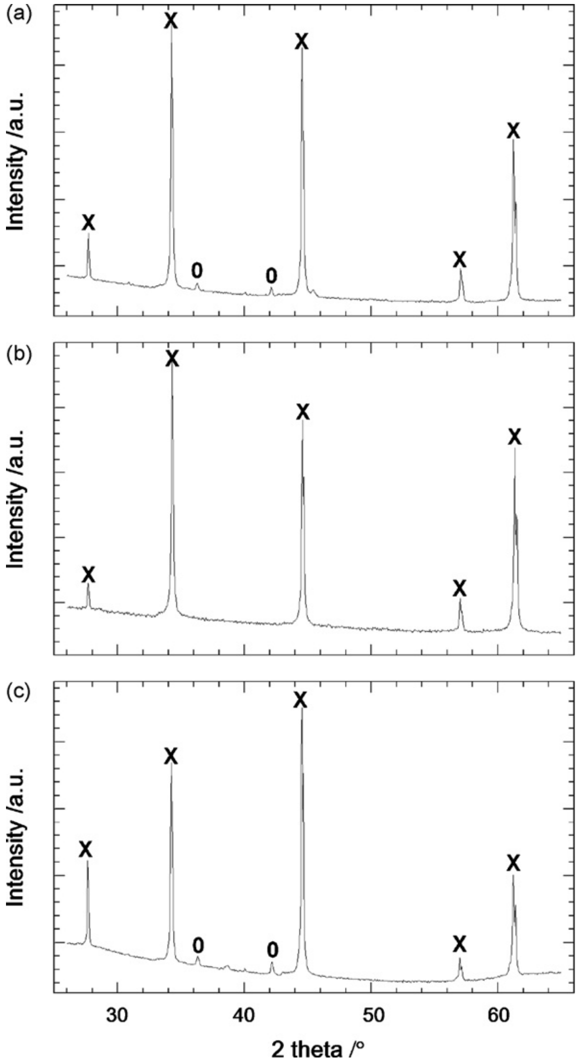

Fig. 4. X-ray diffractograms of the three pristine materials (a) C, (b) H and (c) W. The diffraction lines corresponding to TiB_2 are labeled X and the lines labeled 0 correspond to a secondary phase.

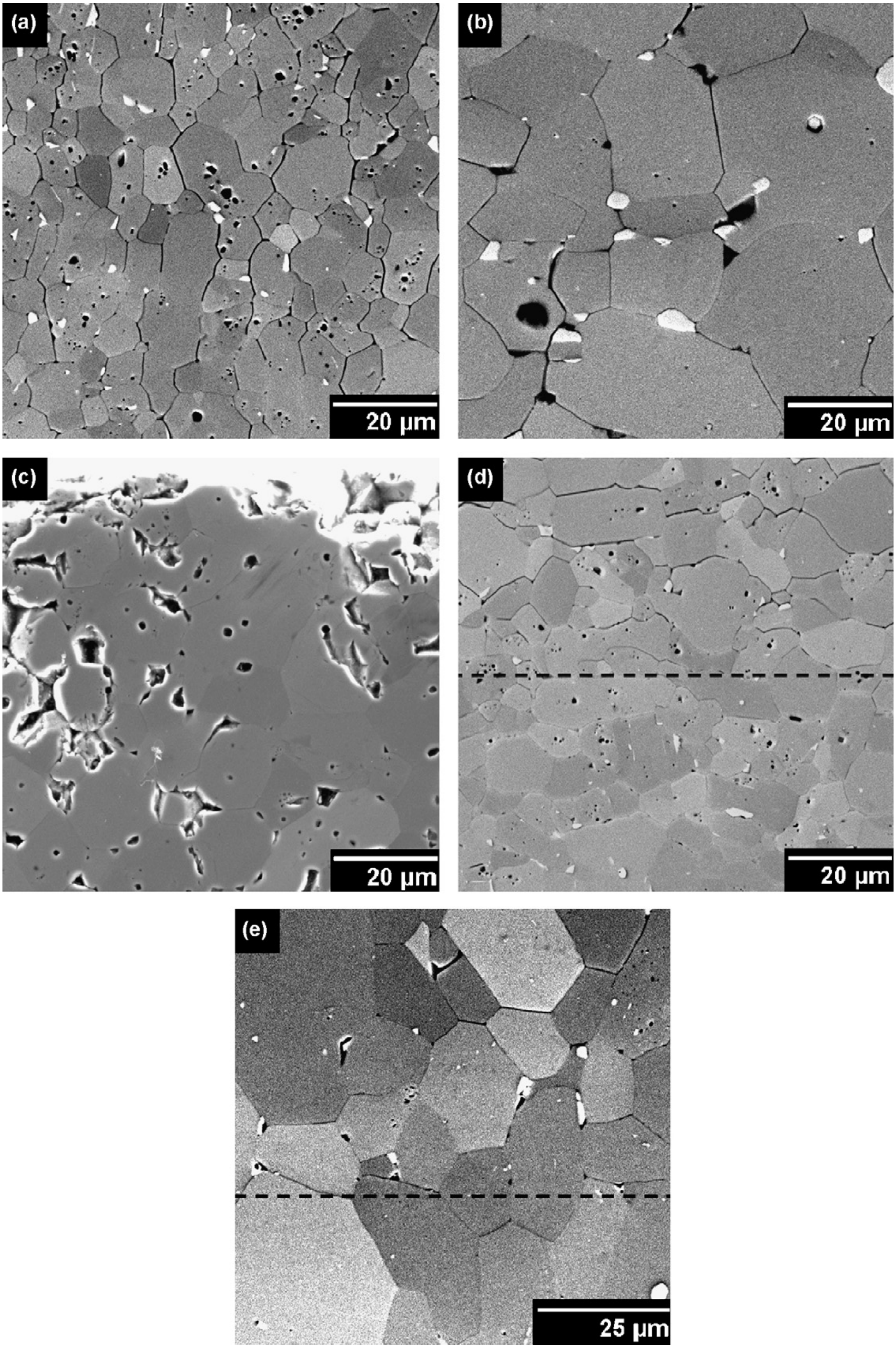

Fig. 5. SEM micrographs (SE) close to the surface of (a) material C after exposure for 2 h, (b) material W after exposure for 24 h, (c) material H after exposure for 100 h, as well as the penetration front (indicated by dashed line) (d) located 0.45 mm from the surface in material C exposed for 2 h, and (e) 0.25 mm from the surface and in material W exposed for 24 h. The surface of the samples is towards the top of the micrographs.

prevent the Al from being smeared out during polishing and hence, chemical analysis could not be used to determine the Al penetration depth. However, comparing the micrographs of the exposed and pristine materials, we observed that the grain boundaries of the exposed materials were mechanically softened during the polishing. For the exposed samples, grain boundaries close to the sample surface were infiltrated by Al and appeared to be mechanically softened and became more pronounced by the polishing, while the interior of the material were similar to the pristine materials. In the following this method were used to determine the penetration depth.

Micrographs of polished cross-sections close to the surface of the exposed materials C, W and H are shown in Fig. 5. For material H, no indication of Al penetration along the grain boundaries could be observed. For materials C and W, the softening of the grain boundaries due to penetration of liquid Al can clearly be seen. The metallic secondary phase present in material C can no longer be seen in the BSE SEM images of the exposed part in Fig. 5. The Ti–O–C–N phase present in both material C and W was however, still present in the infiltrated part of the materials. Any reaction between Al and the Ti–O–C–N phase was not observed by EDS analysis. The penetration front was defined as the boundary between the infiltrated material and the unaffected material after exposure and the penetration depth was defined as the distance from the surface of the sample to the penetration front.

SEM micrographs of the penetration front are included in Fig. 5 for material C after 2 h, exposure and for material W after 24 h, exposure. The degraded material due to penetration of liquid Al can clearly be seen in Fig. 5(d) and (e). For material H, softening of the grain boundaries could not be determined even after 100 h, of exposure.

The penetration of Al along the grain boundaries in TiB_2 can be described by the simple relation in Eq. (1) where x is the penetration depth, D is the grain boundary diffusion coefficient and t is the exposure time.

$$x^2 = Dt \tag{1}$$

The x^2 as a function of the exposure time in liquid aluminum for the three materials are plotted in Fig. 6. The penetration rate was fast for material C, intermediate for material W and slow for material H. The grain boundary diffusion coefficient for penetration of liquid Al estimated from Eq. (1) was 2.5×10^{-11} m^2/s for material C and for material W it was found to be 9.2×10^{-13} m^2/s. For material H the penetration rate is estimated to be $<1.6 \times 10^{-16}$ m^2/s. Clearly the grain boundaries in the three materials have different affinity for liquid Al. We propose that these differences reflect the different chemical composition of the grain boundaries, indicated by the difference of secondary phases in the materials.

The flexural strength and Young's modulus as a function of penetration depth of the exposed material C are shown in Fig. 7. The Young's modulus of the material was clearly decreasing with increasing penetration depth while the flexural strength shows only a small decrease with increasing penetration depth. Mechanical testing could not be performed for the other two materials due to oxidation during exposure to liquid Al.

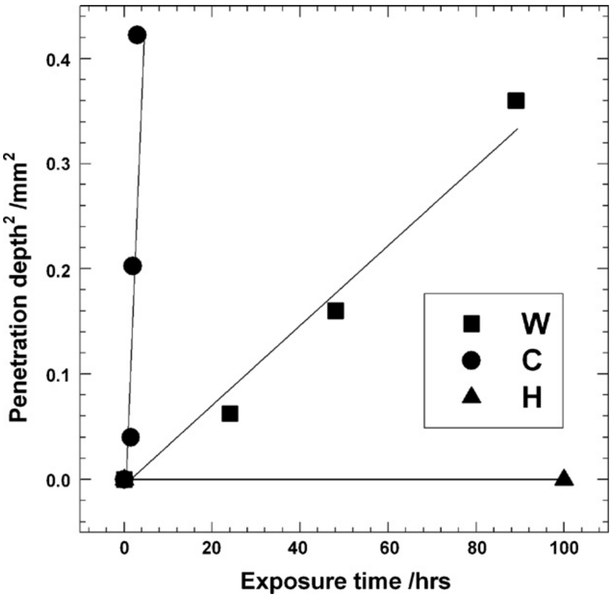

Fig. 6. Penetration depth squared as a function of exposure time for materials C, W and H.

SEM micrographs of the fracture surfaces of pristine and exposed materials are shown in Fig. 8 for materials C, H and W. The micrographs show that the fracture mode changes from mainly intragranular in the pristine materials to intergranular in the infiltrated materials.

The hardness of the C material measured by Vicker's method is presented in Fig. 9. The hardness of the interior of the material, which is not infiltrated by Al, is larger than the hardness of the surface for all the applied loads. The hardness as a function of applied load shows a similar trend for both the bulk and the surface.

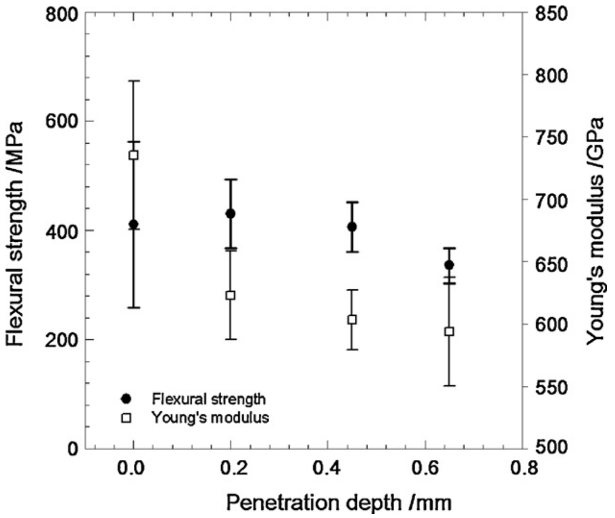

Fig. 7. Flexural strength and Young's modulus as a function of penetration depth for material C.

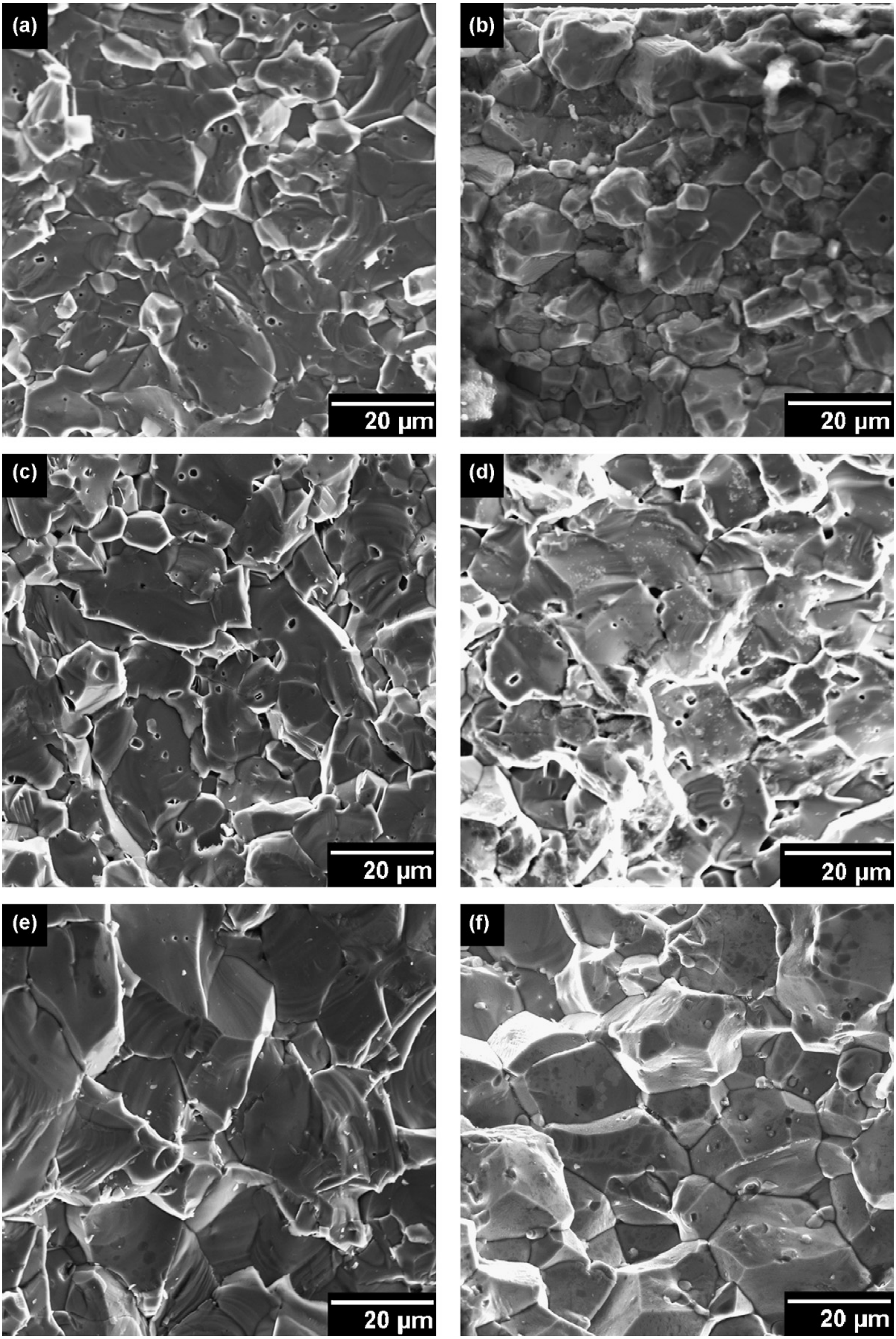

Fig. 8. SEM micrographs of fracture surface of material C (a) before and (b) after exposure to liquid Al, material H (c) before and (d) after exposure to liquid Al and material W (e) before and (f) after exposure to liquid Al.

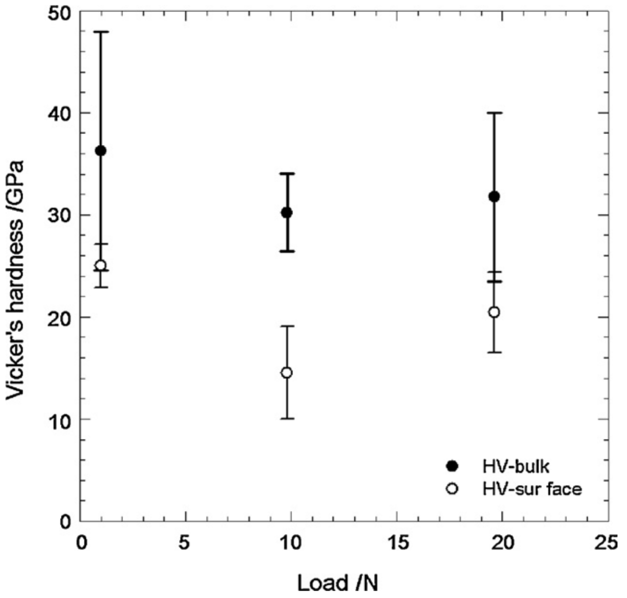

Fig. 9. Vicker's hardness as a function of applied load for material C after exposure to liquid Al.

3.3. Modeling of the stiffness of the materials

The FE model was employed to simulate the degradation of TiB_2 material C by penetration of Al along the grain boundaries. The measured Young's modulus of the pristine material, penetration depths and corresponding flexural strengths of exposed materials were adopted for the simulations. Since the percentage of Al present in the specimens after exposure was not possible to measure quantitatively, a "trial-and-error" method was employed to study the effect of the volume of the infiltrated Al on the stiffness. Stiffness obtained from the numerical simulations was compared with the experimental observations in Fig. 10. The stiffness of the different samples was taken as the slope load versus deflection curves. A decreasing stiffness with increasing Al penetration depth and increasing equivalent volume of Al was the main trend given by the simulations. Using the model given in Fig. 2a, two values for d was employed: $d = 0.3$ and $d = 1.05$ mm. Simulations with $d = 0.3$ and 0.2 mm penetration depth gave a stiffness matching well the experiments and it gave an Al content of 1.9%. Simulations with Al content of 0.6% corresponding to $d = 1.05$ and 0.2 mm penetration depth slightly overestimated the stiffness. Increasing the penetration depth from 0.2 to 0.45 and 0.65 mm resulted in a significant underestimation of the stiffness for $d = 0.3$ mm. Calculations for $d = 1.05$ mm and penetration depths of 0.45 and 0.65 mm resulted in Al contents of 1.38% and 2%, respectively. The modeled stiffness for these Al contents was in accordance with the experiments.

A representative experimental load–deflection curve for each material with a given penetration depth is plotted in Fig. 11 and compared to simulations from the FE analysis. The FE model simulates fairly well the experimental load–deflection curves. The simulations overestimate the stiffness in the case $a = 0.2$ mm and $d = 1.05$ mm as discussed above. The influence of the grain boundary thickness on the simulated stiffness values was analyzed by changing the thickness of the Al grain boundaries in the FE model. The Al content and the penetration depth were kept constant. The considered thicknesses were t and $2t$ (Fig. 2), however, no noticeable difference in the predicted stiffness was observed after changing the thickness of the grain boundaries. The effect of the FE mesh on the results was also studied. The slope of the load–displacement curve was slightly affected by the mesh refinement level. Further refinement of the present model showed no significant change of the results. Therefore the used FE model was regarded as sufficient for the present purpose. In addition, the stress distribution in the penetrated material was studied. The stress levels obtained from the FE analysis using both models in Fig. 2a and b, are about or below the yield

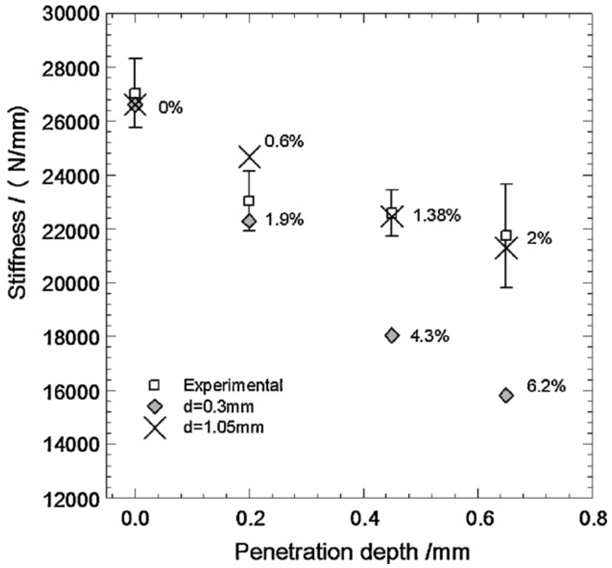

Fig. 10. Material stiffness from FE simulations compared to experimental values for material C. Al content percentage is given in the figure for the stiffness values from FE simulations.

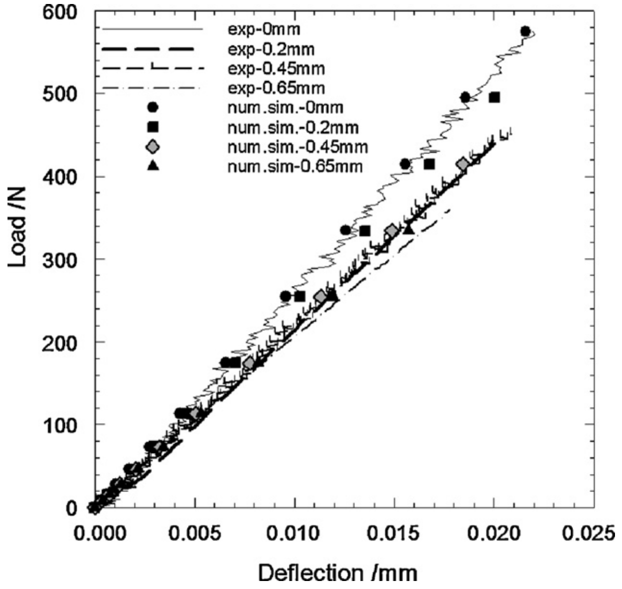

Fig. 11. Experimental load–displacement curves for material C with different Al penetration depths compared to data from FE simulations.

stress value of aluminum alloys[24] confirming the assumed elastic behavior of Al.

4. Discussion

4.1. Infiltration of liquid aluminum in TiB_2

The investigation of the microstructure of the three different TiB_2 materials before and after exposure to liquid Al shows that they are vulnerable to degradation due to infiltration of Al in the form of penetration along the grain boundaries. The penetration causes a weakening of the grain boundary cohesion and possibly cracking, pull out of grains and failure of the TiB_2 cathode during electrolysis. There are several possible mechanisms for the infiltration of Al along grain boundaries in a polycrystalline ceramic material. For the first, wetting of the grain boundaries will occur if the TiB_2 grain boundary interfacial energy is twice that of the Al–TiB_2 interfacial energy. The interfacial energy may change due to impurities segregated to the grain boundaries, temperature and crystallography. Due to the low solubility of TiB_2 in liquid Al, elastic strains will build up upon penetration of Al along the grain boundaries. This will either impede the penetration, or result in cracking of the material. Secondly, infiltration of the grain boundaries will result if there is a reduction of internal strain due to the anisotropic thermal expansion after infiltration. Further, penetration through open porosity in the material or through microcracks is a possible infiltration mechanism. Lastly, penetration due to reactions with a secondary phase is possible. The penetration in a material with a secondary phase which is soluble in Al (e.g. metal) will be driven by diffusion, while the penetration in a material with a secondary phase not coexistent or soluble in Al (e.g. refractory oxide such as TiO_2) will be driven by the chemical reaction between the secondary phase and Al (e.g. $Al + TiO_2 = Al_2O_3 + Ti$). If the reaction between the secondary phase and Al forms a phase with increased molar volume, internal stresses will build up and possibly induce crack formation and by this way increase the rate of degradation. Such effect has been reported for the reaction $4Al + 3TiC = Al_4C_3 + 3Ti$.[28] The distribution of the secondary phase will also influence the penetration rate. Hence, the penetration rate will be dependent on both the nature and the distribution of the secondary phase.

The materials investigated in this study which has been infiltrated by Al during the exposure experiments contained secondary phases and hence the penetration involved reactions with the secondary phases. Material C was penetrated due to the dissolution of the metallic secondary phase as there were no sign of this phase after penetration of Al. TiB_2 materials with metallic secondary phases exposed to Al have been shown to be readily infiltrated in earlier studies.[16]

Material W was probably penetrated due the reaction between Al and the Ti–N–C–O phase, however, any formation of a Ti–N–C–O–Al phase due this reaction was not observed by EDS. It is possible, however, that only the outermost layer of the Ti–N–C–O phase reacted with the Al. After exposure of TiB_2 with several oxide impurities Pettersen,[28] e.g. found that a Ti(CNO) phase present prior to exposure was partly reacted with Al after exposure. An α-Al_2O_3 phase was also found in the same sample and Ti_2O_3 was proposed to be the main oxygen source for the alumin formation. Penetration due to reaction between Al and oxide secondary phases has also been identified by Nord-Varhaug[17] who found α-Al_2O_3 and β-Al_2O_3 in triple junctions and an $(Al_2OC)_{1-x}(AlN)_x$ phase surrounding the grains after exposure of TiB_2 with SiO_2 as the main oxide impurity phase. The SiO_2 was believed to be the oxygen source for the alumina formation, however the source for $(Al_2OC)_{1-x}(AlN)_x$ was not determined. Gesing and Wheeler[29] reported formation of Al_2O_3 in a material containing oxide impurities on grain boundaries and formation of Al_4C_3 in materials containing C in triple junctions.

In this study the rate of penetration of Al in the material with the metallic secondary phase is higher than the rate of penetration in the material with the Ti–N–C–O phase. However, material H with no secondary phase observed shows superior resistance to Al penetration. Thus it seems that the grain boundary chemistry is more important than the density and the strength of a TiB_2 material used as a cathode during Al electrolysis.

4.2. Influence of the infiltration on the mechanical properties

The mechanical properties of TiB_2 are degraded by infiltration of liquid Al as shown for material C. A decrease of stiffness and Young's modulus of TiB_2 was observed as the Al penetration depth increased (Fig. 7). The stiffness of the penetrated material is a function of Young's modulus of TiB_2, the Young's modulus of Al, the amount of Al and the penetration depth along the grain boundaries. The role of aluminum, a ductile material, is to soften TiB_2. Therefore Al-infiltrated TiB_2 responds to the same applied load with a larger deflection than pristine TiB_2 (Fig. 11). This change of load–deflection behavior was well simulated by the FE model. The infiltrated material also presents a lower Vicker's hardness than pristine material. As hardness is a measure of plastic deformation during indentation, material infiltrated with Al is more prone to local deformation.

The flexural strength of TiB_2 also seems to decrease by increasing the Al penetration depth. The decrease is however not so pronounced probably due to a crack bridging effect of the ductile Al along the grain boundaries as the penetrated materials show intergranular fracture mode. There is a change in grain boundary cohesion at room temperature giving a change from transgranular to intergranular fracture mode after penetration of Al. At elevated temperatures, the grain boundary cohesion will be significantly lower since the Al present at the grain boundaries will be in the liquid state. A change of fracture mode from transgranular to intergranular due to Pb infiltration in an Al alloy has also been reported.[30]

4.3. Potential for inert cathodes based on TiB_2

Finch[11] measured the solubility of Ti and B in liquid Al at temperatures between 800 and 1300 °C. A solubility product of $\sim 1 \times 10^{-8}$ for TiB_2 in liquid Al at 960 °C was reported. Based on this, Thonstad et al.[31] estimated a wear rate of ∼0.2 mm/year for a commercial electrolysis cell. A degradation rate of this order would be of no concern for a massive TiB_2 cathode. However, as shown in this study, the degradation of TiB_2 is determined by the infiltration of Al along the grain boundaries and not dissolution of the TiB_2 material itself. Assuming detachment of grains from the electrode in the infiltrated material, the degradation rate would be ∼60 mm/year for material W and ∼1900 mm/year for material C, which is well above acceptable values.

5. Conclusions

Polycrystalline TiB_2 ceramics with secondary phases were penetrated by aluminium during exposure in liquid aluminium at 1000 °C. The penetration rate depended especially on the presence and distribution of secondary phases at the grain boundaries and triple junctions while density, porosity and grain size were shown to be of less importance. After penetration of Al, the stiffness, Young's modulus, hardness and flexural strength of the material were reduced and the fracture mode changed from transgranular to intergranular. A FE model was developed to simulate the stiffness decrease in TiB_2 due to the presence of Al. The stiffness of TiB_2 was predicted as a function of the penetration depth and the Al equivalent volume content. The FE model showed that the equivalent volume percentage of Al in the specimen affected largely the stiffness of the penetrated material. The FE simulation showed results in accordance with the experiments.

Acknowledgement

This study was supported by The Research Council of Norway through the project "Thermodynamics Applied to High Temperature Materials Technology".

References

1. Sørlie, M. and Øye, H. A., *Cathodes in Aluminium Electrolysis* (*2nd ed.*). Aluminium-Verlag, Dusseldorf, 1994.
2. Boxall, L. G., Cooke, A. V. and Hayden, H. W., Light metals 1984. *The Metallurgical Society of AIME*. Warrendale, Pennsylvania, 1984, pp. 573–588.
3. Billehaug, K. and Øye, H. A., Inert cathodes for aluminum electrolysis in Hall–Héroult cells. Pt. I. *Aluminium*, 1980, **56**(10), 642–648.
4. Billehaug, K. and Øye, H. A., Inert cathodes for aluminum electrolysis in Hall–Héroult cells. Pt. II. *Aluminium*, 1980, **56**(11), 713–718.
5. Baumgartner, H. R. and Steiger, R. A., Sintering and properties of titanium diboride made from powder synthesizes in a plasma-arc. *J. Am. Ceram. Soc.*, 1984, **67**(3), 207–212.
6. Einarsrud, M.-A., Hagen, E., Pettersen, G. and Grande, T., Pressureless sintering of titanium diboride with nickel, nickel boride, and iron additives. *J. Am. Ceram. Soc.*, 1997, **80**(12), 3013–3020.
7. Finch, C. B., Effect of impurities on the densification of submicrometer TiB_2 powders. *Adv. Ceram. Mater.*, 1986, **1**(1), 50.
8. Tennery, V. J., Finch, C. B., Yust, C. S. and Clarck, G. W., In *Structure–Property Correlations for TiB_2-based Ceramics Densified Using Active Liquid Metals*, ed. R. K. Viswanadham, D. J. Rowcliff and J. Gurland. Plenum Publishing Corp., New York, 1983.
9. Evans, A. G., Microfracture from thermal-expansion anisotropy. 1. Single-phase systems. *Acta Metall.*, 1978, **26**(12), 1845–1853.
10. Pezzotta, M., Zhang, Z. L., Jensen, M., Grande, T. and Einarsrud, M.-A., Cohesive zone modeling of grain boundary microcracking induced by thermal anisotropy in titanium diboride ceramics. *Comp. Mater. Sci.*, 2008, **43**(3), 440–449.
11. Finch, N. J., The mutual solubilities of titanium and boron in pure aluminum. *Metall. Mater. Trans. B, Process Metall. Mater. Process. Sci.*, 1972, **3**(10), 2709–2711.
12. Bannister, M. K. and Swain, M. V., A preliminary investigation of the corrosion of a TiB_2/BN/AIN composite during aluminium evaporation. *Ceram. Int.*, 1989, **15**(6), 375–382.
13. Baumgartner, H. R., Subcritical crack velocities in titanium diboride under simulated Hall–Heroult cell conditions. *Am. Ceram. Soc. Bull.*, 1984, **63**(9), 1172–1175.
14. Baumgartner, H. R., Mechanical properties of densely sintered high-purity titanium diborides in molten aluminum environments. *J. Am. Ceram. Soc.*, 1984, **67**(7), 490–497.
15. Dorward, R. C., Aluminium penetration and fracture of titanium diboride. *J. Am. Ceram. Soc.*, 1982, **65**(1), C6.
16. Finch, C. B. and Tennery, V. J., Crack formation and swelling of TiB_2–Ni ceramics in liquid aluminum. *J. Am. Ceram. Soc.*, 1982, **65**(7), C100–C101.
17. Nord-Varhaug, K. K., TEM investigation of impurity phases and the penetration of liquid aluminum in hot isostatically pressed TiB_2 compacts. *J. Am. Ceram. Soc.*, 1996, **79**(5), 1147–1154.
18. Zdaniewski, W. A., Role of microstructure and intergranular phases in stress corrosion of TiB_2 exposed to liquid aluminum. *J. Am. Ceram. Soc.*, 1985, **68**(11), 309–312.
19. Zdaniewski, W. A., Degradation of hot-pressed TiB_2–TiC composite in liquid aluminium. *Am. Ceram. Soc. Bull.*, 1986, **65**(10), 1408–1414.
20. Zdaniewski, W. A., Effect of segregated Cr on degradation of (Ti, Cr)B_2 exposed to liquid aluminium. *J. Electrochem. Soc.*, 1986, **133**(9), 1777–1781.
21. Joseph, B., Picat, M. and Barbier, F., Liquid metal embrittlement: a state-of-the-art appraisal. *EPJ Appl. Phys.*, 1999, **5**(1), 19–31.
22. Chen, C. R., Pascual, J., Fischer, F. D., Kolednik, O. and Danzer, R., Prediction of fracture toughness of a ceramic multilayer composite—modeling and experiments. *Acta Mater.*, 2007, **55**(2), 409–421.
23. Chawla, N. and Sidhu, R. S., Microstructure-based modeling of deformation in Sn-rich (Pb-free) solder alloys. *J. Mater. Sci.: Mater. Electron.*, 2007, **18**(1–3), 175–189.
24. Benham, P. P., Crawfords, R. J. and Armstrong, C. G., *Mechanics of Engineering Materials* (*2nd ed.*). PAddison Wesley Longman Limited, Essex, 1996.
25. Munro, R. G., Material properties of titanium diboride. *J. Res. Nat. Inst. Stand. Technol.*, 2000, **105**(5), 709–720.
26. Afir, A., Achour, M. and Saoula, N., X-ray diffraction study of Ti–O–C system at high temperature and in a continuous vacuum. *J. Alloys Compd.*, 1999, **288**(1/2), 124–140.
27. Jensen, M. S., Einarsrud, M.-A. and Grande, T., Preferential grain orientation in hot pressed TiB_2. *J. Am. Ceram. Soc.*, 2007, **90**(4), 1339–1341.
28. Pettersen, G., *Development of microstructure during sintering and aluminium exposure of titanium diboride ceramics*. Dr. Ing. Thesis, Norwegian University of Science and Technology, Department of Physics, Trondheim, 1997.
29. Gesing, A. J. and Wheeler, D. J., In *Screening and Evaluation Methods of Cathode Materials for use in Aluminum Reduction Cells in Presence of Molten Aluminum and Cryolite up to 1000 °C, in Light Metals, AIME Annual Meeting*, 1987, pp. 327–334.
30. Wouters, O. and De Hosson, J. Th. M, Lead induced intergranular fracture in aluminum alloy AA6262. *Mater. Sci. Eng.*, 2003, **A361**(1–2), 331–337.
31. Thonstad, J., *Aluminium Electrolysis: Fundamentals of the Hall–Héroult process*. Aluminium-Verlag, Düsseldorf, 2001, p. 359.